Journal of Operation and Automation in Power Engineering

vol. 13, no. Special Issue, Dec. 2025, Pages: 29-43

http://joape.uma.ac.ir

Research Paper

Dynamic Modeling and State Feedback Control for Enhancing Small Signal Stability in Islanded Microgrids with Diesel Generator Frequency Damping

Shakhboz Meylikulov [1, *], *Isayev Fakhriddin* [2], *Kochkarova Madina* [3], *Turayev Muhammadi* [4], *Zakirjon Musabekov* [5], *Ochilov Farxodjon* [6], and *Ulugbek Anarboyevich Nurmanov* [7]

[1] *Termez University of Economics and Service, Termez, Uzbekistan.*
[2] *Scientific Research Center Scientific Foundations and Problems of the Development of the Economy of Uzbekistan under Tashkent State University of Economics, Tashkent, Uzbekistan.*
[3] *Turin Polytechnic University in Tashkent, Tashkent, Uzbekistan.*
[4] *Kattakurgan State Pedagogical Institute, Samarkand, Uzbekistan.*
[5] *Tashkent State Technical University named after Islam Karimov, Tashkent, Uzbekistan.*
[6] *Tashkent State University of Economics, Tashkent, Uzbekistan.*
[7] *The Banking and Finance Academy of the Republic of Uzbekistan.*

Abstract— *Microgrids face significant challenges due to the stochastic behavior of distributed energy resources, which may excite low-damped oscillatory modes and compromise stability. This paper develops a unified small-signal model of an islanded microgrid and proposes a state-feedback controller (SFC) as a power system stabilizer (PSS) to enhance low-frequency damping in the diesel generator subsystem. The controller and inverter control parameters are tuned using a genetic algorithm (GA). Numerical results show that the proposed approach increases the damping ratio of the dominant electromechanical mode from 0.03 to 0.18 (a six-fold improvement) and reduces rotor-speed overshoot by nearly 60% under a 10% disturbance. Time-domain simulations further confirm a 70% reduction in settling time for rotor-angle deviations. These results demonstrate that the optimized SFC significantly improves electromechanical damping and strengthens the small-signal stability margin of the islanded microgrid.*

Keywords—Islanded microgrid, small-signal stability, state-feedback controller, power system stabilizer, genetic algorithm, diesel generator dynamics.

1. INTRODUCTION

In recent years, the increasing penetration of distributed energy resources (DERs) [1]—such as photovoltaic systems [2], wind turbines [3], vortex induced vibration [4], and microturbines—has transformed the traditional centralized power grid into a more decentralized and flexible structure known as the microgrid [5, 6]. A microgrid can operate either in grid-connected or islanded mode, providing enhanced reliability, energy efficiency, and resilience against grid disturbances. However, the islanded mode of operation introduces significant challenges related to voltage and frequency regulation, power-sharing, and particularly small-signal stability, due to the absence of a strong grid reference and the dynamic interactions among multiple converter-based units.

Received: 27 Nov. 2025
Revised: 23 Dec. 2025
Accepted: 25 Dec. 2025
*Corresponding author:
E-mail: shaxboz_meyliqulov@tesu.uz (S. Meylikulov)
DOI: 10.22098/joape.2025.18912.2465

The stochastic and intermittent nature of renewable energy generation causes frequent fluctuations in active and reactive power outputs [7]. These variations can lead to low-frequency oscillations (LFOs), voltage instability, and reduced damping performance within the microgrid [8, 9]. Consequently, maintaining stable operation under such uncertain and dynamic conditions necessitates the implementation of advanced control strategies capable of providing robust stability and adequate damping characteristics. To address these challenges, various control methodologies have been proposed in the literature [10], including droop control, model predictive control (MPC), and adaptive or robust control schemes [11]. Nevertheless, these methods often face limitations when dealing with system nonlinearities and parameter uncertainties in inverter-based microgrids. In this context, state feedback control (SFC) emerges as a powerful tool that allows direct placement of system poles, thereby improving both dynamic response and small-signal stability. A dynamic model of an inverter-based distributed generator specifically designed for small-signal stability analysis was presented in [12]. The study emphasized the influence of the inverter's inner current and voltage control loops, power control, and phase-locked loop (PLL) dynamics on the overall system stability. Furthermore, reference [13] highlighted the critical role of system architecture, diversity of energy sources, and energy storage elements in determining the microgrid's dynamic performance and stability margins.

Several studies have examined stability enhancement in islanded microgrids using various control approaches [14, 15]. Prior work has investigated load–frequency control strategies [16], adaptive damping control for DC microgrids [17], resonance analysis and stability conditions [18], and the dynamics of wind–diesel hybrid systems [19]. Other contributions have explored virtual inertia and advanced feedback strategies [20, 21], as well as optimal damping control in diesel-based microgrids [22, 23]. While these studies provide valuable insights, most of them treat inverter controllers and stabilizing controllers separately or rely on simplified droop-based models. A unified small-signal framework that explicitly captures diesel–inverter interactions and enables coordinated stabilizer tuning remains insufficiently addressed in the literature. Recent studies have also introduced advanced frequency-control mechanisms for islanded and interconnected microgrids that highlight the need for more robust stabilization strategies. Shayeghi *et al.* [24] proposed a multi-objective optimized parallel FOPI–FPOD controller for enhancing LFC performance in islanded microgrids, demonstrating strong robustness against sudden load variations, RES intermittency, and parametric uncertainties. In a related direction, Shayeghi *et al.* [25] developed the TIDA+1 error-signal regulator, combining tilt, integrator, derivative, and acceleration operators within a PSO-optimized framework to improve LFC behavior in interconnected microgrids under modeling uncertainties and nonlinearities. These contributions emphasize the increasing reliance on optimized and multi-operator controllers for frequency stabilization; however, they primarily target LFC rather than the small-signal electromechanical stability challenges addressed in the present work. Unlike these methods, the proposed study develops a unified small-signal model and a state-feedback damping controller specifically designed to reshape dominant oscillatory modes in diesel-supported islanded microgrids. In addition to microgrid-oriented stabilizing methods, several studies have investigated nonlinear control strategies aimed at enlarging the domain of attraction of dynamical systems. Yadipour *et al.* [26] proposed a Lyapunov-based controller design framework grounded in Zubov's theorem to stabilize a class of affine nonlinear systems and systematically expand their domain of attraction. Their results, demonstrated on the Van der Pol oscillator and a non-globally stabilizable system, highlight the importance of robust nonlinear stabilization in improving system reliability.

Beyond power system applications, several recent studies in mechanical and robotic systems also demonstrate the effectiveness of optimization-based design strategies for improving dynamic performance [27]. Bingham *et al.* [28] investigated advanced material selection and the design of lightweight, high-strength robotic structures inspired by natural geometries, showing how additive manufacturing and experimental characterization can enable enhanced mechanical efficiency. Similarly, Yancheshmeh *et al.* [29] applied finite element analysis combined with genetic algorithms to optimize autonomous vehicle chassis design under complex loading scenarios, achieving improved weight–strength balance and structural robustness. Although these works focus on mechanical systems rather than microgrids, they highlight the broader applicability of evolutionary optimization methods—such as GA—in achieving superior system performance. This perspective supports the motivation behind our use of GA for coordinated controller tuning in the proposed microgrid stabilization framework. Although previous studies have explored various damping controllers and inverter control strategies, several limitations remain. Conventional PSS designs rely primarily on rotor-speed input and torsional filters, which introduce undesirable phase lag at low frequencies and reduce damping of excitation modes. Many inverter-based microgrid studies employ simplified droop or reduced-order inverter models, preventing accurate representation of the coupled electromechanical–converter dynamics. Moreover, stabilizers and inverter controllers are typically tuned independently, without ensuring coordinated behavior across the diesel generator and IBDG. Few works provide a unified small-signal model that integrates the diesel generator, AVR, full inverter control loops, and the network in a common reference frame. These limitations motivate the need for a more comprehensive modeling framework and a multi-state feedback stabilizer capable of directly shaping the dominant oscillatory modes. Despite the extensive literature on microgrid stability, two major limitations remain. First, most existing studies model the diesel generator, inverter control loops, and the network separately, without constructing an integrated small-signal model that captures their coupled dynamics. Second, stabilizer design is typically performed independently of inverter control tuning, limiting the achievable damping improvements. These gaps highlight the need for a unified modeling framework and a coordinated tuning methodology capable of jointly optimizing both inverter controllers and stabilizers. To clearly position the proposed work within the existing body of literature, a taxonomy-based comparison is provided in Table 1. This structured comparison highlights that most existing approaches rely on simplified or decoupled models and independently tuned controllers, whereas the proposed method uniquely combines a unified small-signal model with a coordinated GA-optimized state-feedback stabilizer. The taxonomy therefore clarifies the methodological gap addressed by this study and motivates the proposed control framework.

In this study, a comprehensive dynamic model of an islanded microgrid is developed to accurately capture the coupled dynamics of inverter-based DERs and a diesel generator. The proposed state feedback controller is designed and tuned to act as a power system stabilizer (PSS), aiming to mitigate low-frequency oscillations and enhance overall damping performance. Furthermore, the controller parameters are optimized using a GA to ensure superior stability margins and adaptability to varying operating conditions. The effectiveness of the proposed approach is validated through time-domain simulations and eigenvalue-based small-signal analysis, demonstrating that the optimized SFC can significantly improve the microgrid's transient and steady-state performance. The findings highlight the potential of the proposed control strategy as a viable solution for achieving reliable and stable operation of islanded microgrids with high penetration of inverter-based resources. The main contributions of this work can be summarized as follows:

1) A unified small-signal model that integrates the diesel generator, AVR, and full inverter control loops in a common DQ frame;
2) A multi-state feedback PSS that avoids torsional filters and enables direct eigenvalue placement;
3) A coordinated GA-based method that jointly optimizes inverter control gains and PSS feedback parameters using eigenvalue-oriented criteria; and
4) Verified improvements in damping, overshoot, settling time, and overall small-signal stability through eigenvalue analysis and time-domain simulations.

This work addresses the above gap through the following contributions: (i) developing a unified small-signal state-space model combining diesel generator, AVR, and full inverter control loops; (ii) designing a multi-state feedback PSS that avoids torsional filtering; and (iii) proposing a coordinated GA-based optimization that simultaneously tunes inverter control gains and PSS feedback parameters based on eigenvalue-oriented criteria.

2. Small-Signal Modeling of the Islanded Microgrid

The component models employed in this work for the diesel generator, its excitation system, the inverter-based distributed generator, and the network follow standard representations widely adopted in the literature on microgrid dynamics and small-signal analysis. Rather than introducing entirely new device-level models, the contribution of this section is to assemble these established subsystems into a unified small-signal state-space framework expressed in a common DQ reference frame. This integrated formulation explicitly includes the dynamics of the AVR, the

Table 1. Comparison of literature review.

Reference	Microgrid type	Dynamic model	Stabilization method	Diesel–inverter coordination	Optimization method	Key limitation
[12]	Islanded	Inverter-only small-signal	Inner-loop control tuning	No	None	Diesel dynamics neglected
[17, 18]	Wind–diesel	Reduced-order	Conventional PSS	Partial	None	Simplified inverter model
[20, 21]	Islanded	Averaged model	Virtual inertia / damping	No	Heuristic tuning	Limited damping of electromechanical modes
[22, 23]	Diesel-based	Generator-focused	Optimal PSS	No	GA / PSO	Inverter dynamics ignored
[24]	Islanded	LFC-oriented	Parallel FOPI–FPOD	No	Multi-objective optimization	Targets frequency control, not small-signal modes
[25]	Interconnected	LFC-oriented	TIDA+1 regulator	No	PSO	Not eigenvalue-based
This work	**Islanded**	**Unified diesel–inverter small-signal model**	**Multi-state feedback PSS**	**Full coordination**	**GA (eigenvalue-based)**	**–**

inverter's power/voltage/current control loops, and the network interconnection, thereby providing a consistent basis for eigenvalue-based stability assessment and for the state-feedback controller design presented in Section 3. One of the key characteristics of a microgrid is its ability to operate in two distinct modes: grid-connected and islanded (stand-alone). In the islanded mode of operation, the microgrid is disconnected from the main utility grid, and the distributed generation (DG) units are solely responsible for supplying the total power demand of the local loads. Under this condition, the voltage and frequency of the microgrid must be regulated within acceptable limits, despite the absence of grid support.

In islanded operation, each distributed energy resource—particularly inverter-based units—plays a crucial role in maintaining stable voltage and frequency levels. To achieve this, decentralized control strategies are typically employed, relying exclusively on locally measured quantities such as voltage, current, and power. In this study, an entirely local control scheme is adopted for the inverter-interfaced DG, enabling fully autonomous operation and improved power sharing within the islanded microgrid. The proposed small-signal model of the studied microgrid, illustrated schematically in Fig. 1, decomposes the system into four major subsystems:

1) Diesel Generator Subsystem,
2) Inverter-Based Distributed Generation Subsystem,
3) Network (Distribution Line) Subsystem, and
4) Load Subsystem.

Each subsystem is represented by a set of nonlinear differential and algebraic equations that describe its dynamic behavior. These equations are subsequently linearized around a nominal operating point to obtain a unified state-space representation of the islanded microgrid. This formulation enables systematic small-signal stability analysis through eigenvalue computation and facilitates the design of advanced, damping-oriented control strategies aimed at improving both dynamic response and overall stability.

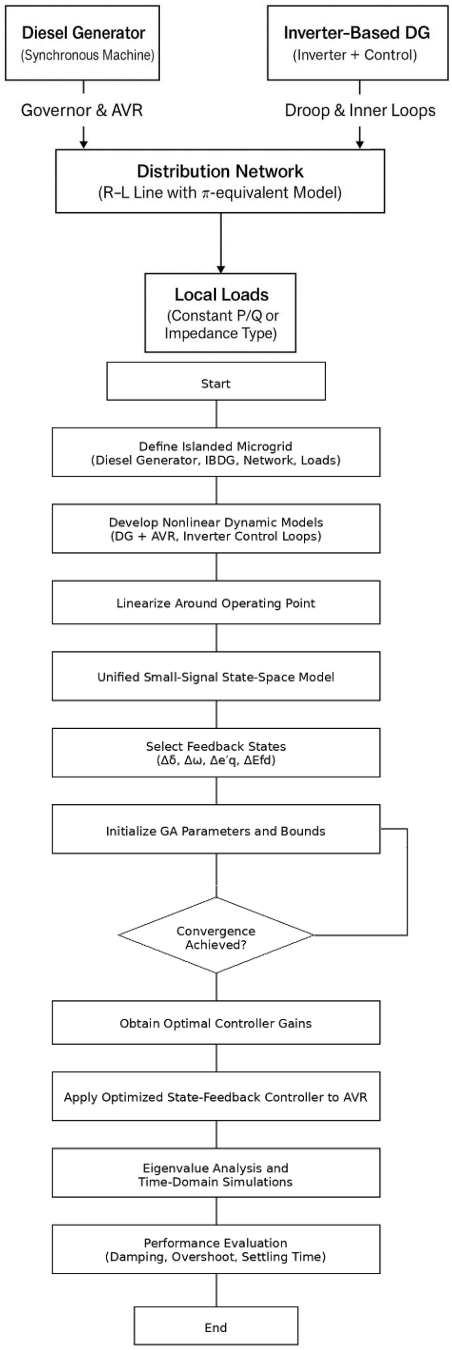

Fig. 1. Simplified schematic representation of the islanded microgrid model.

2.1. Reference frame transformation and model integration

Each DG unit in the microgrid is modeled in its own synchronous reference frame (dq-frame). The inverter-based DG is represented in the reference frame aligned with its internal voltage vector, while the diesel generator dynamics are expressed in the rotor reference frame of the synchronous machine. The dynamic model of the inverter-based DG includes the power control loops, output filter dynamics, coupling inductor, and the voltage and current controllers. These control loops collectively regulate the active and reactive power delivered to the microgrid and maintain stable voltage and frequency during islanded operation.

In this study, the network and load dynamics are expressed in the reference frame of the diesel generator, which serves as the common reference for the entire system. To integrate the inverter-based DG model with the rest of the system, a reference frame transformation is applied to align its state variables with the diesel generator reference frame. This transformation is achieved using a rotational transformation matrix, as shown in Eq. (1) [30]:

$$\begin{bmatrix} \cos(\delta) & \sin(\delta) \\ -\sin(\delta) & \cos(\delta) \end{bmatrix} \begin{bmatrix} x_{d'} \\ x_{q'} \end{bmatrix}_{INV} \tag{1}$$

where δ represents the angular displacement between the inverter's reference frame and the diesel generator reference frame.

The transfer function matrix that relates the inverter-based DG variables to the common reference frame is defined as [30]:

$$G(s) = \begin{bmatrix} G_{dd}(s) & G_{dq}(s) \\ G_{qd}(s) & G_{qq}(s) \end{bmatrix} \tag{2}$$

This matrix describes the dynamic coupling between the d- and q-axis components of voltage and current, and it enables the unified representation of both generation subsystems in a single coordinated model. The transformed equations facilitate the formulation of a comprehensive state-space model for the islanded microgrid, suitable for small-signal stability analysis and controller design.

2.2. State–space model of the diesel generator

The linear model of the DG is formulated following standard synchronous machine and excitation system representations. Parameter values are listed in Table 2. The stator voltage equations in the synchronous dq-frame are expressed in terms of the transient internal voltages e'_d, e'_q and stator currents I_d, I_q as shown in [30]:

$$\begin{aligned} V_d &= e_{d'} - R_a I_d - X_q I_q, \\ V_q &= e_{q'} - R_a I_q + X_d I_d, \end{aligned} \tag{3}$$

where I_d and I_q are stator currents; e'_d and e'_q are transient EMFs; v_d and v_q are terminal voltages; and R_a, X'_d, X'_q denote stator resistance and d–q transient reactances. The instantaneous active and reactive powers P and Q are expressed as functions of e'_d, e'_q, I_d, and I_q according to:

$$\begin{aligned} P &= e_{d'} I_d + e_{q'} I_q, \\ Q &= e_{q'} I_d - e_{d'} I_q. \end{aligned} \tag{4}$$

The rotor swing dynamics and the transient q-axis electromotive force (EMF) are modeled using the relationships between rotor angle δ, angular velocity ω, mechanical input power P_m, electrical output power P_e, damping coefficient D, and inertia constant M as given in [30]:

$$\begin{aligned} \dot{\delta} &= \omega - \omega_0, \\ \dot{\omega} &= \tfrac{1}{M}(P_m - P_e - D(\omega - \omega_0)), \end{aligned} \tag{5}$$

$$\dot{e}_{q'} = \frac{1}{T_{d0'}} \left(-e_{q'} - (X_d - X_{d'}) I_d + E_{fd}\right), \tag{6}$$

where δ is rotor angle, ω is rotor speed, M is inertia constant, D is damping coefficient, P_m is mechanical input power, and P_e is electrical output power.

Table 2. Parameters of the diesel generator.

Parameter	Value	Parameter	Value
P (kW)	21	V (V)	224
R_a (p.u.)	4.41	D	1.21
T_A (s)	4.42	K_A	0.417
$T_{d'0}$ (s)	4.417	$T_{q'0}$ (s)	4.42
X_d (p.u.)	1.30	X'_d (p.u.)	1.18
X_q (p.u.)	4.71	X'_q (p.u.)	4.12

The excitation system of the diesel generator is represented by an automatic voltage regulator (AVR), in which the field voltage E_{fd} is controlled according to the voltage reference V_{ref} and the terminal voltage V_t through the gain K_A and time constant T_A:

$$\dot{E}_{fd} = \frac{1}{T_A} \left(-E_{fd} + K_A (V_{\text{ref}} - V_t)\right). \tag{7}$$

The small-signal state, input, and output vectors of the diesel generator are defined as:

$$\begin{aligned} \Delta X_G &= \begin{bmatrix} \Delta\omega & \Delta\delta & \Delta e_{q'} & \Delta E_{fd} \end{bmatrix}^T, \\ \Delta V_{dqG} &= \begin{bmatrix} \Delta V_d & \Delta V_q \end{bmatrix}^T, \\ \Delta I_{dqG} &= \begin{bmatrix} \Delta I_d & \Delta I_q \end{bmatrix}^T. \end{aligned} \tag{8}$$

Around an equilibrium operating point, the linearized dynamic equations of the DG can be written in the compact state-space form:

$$\begin{aligned} \Delta \dot{X}_G &= A_G \Delta X_G + B_G \Delta V_{b,DQG}, \\ \Delta I_G &= C_G \Delta X_G + D_G \Delta V_{b,DQG} \end{aligned} \tag{9}$$

where $\Delta V_{b,DQG}$ represents the small perturbations of the bus voltage at the DG terminals in the DG dq-reference frame.

To integrate the DG with the rest of the microgrid model, the reference-frame transformation matrix $T_s(\delta_0)$ and its inverse $T_s^{-1}(\delta_0)$ are used to map variables between coordinate systems:

$$\begin{aligned} T_s(\delta_0) &= \begin{bmatrix} \cos\delta_0 & \sin\delta_0 \\ -\sin\delta_0 & \cos\delta_0 \end{bmatrix}, \\ T_s^{-1}(\delta_0) &= T_s^{\top}(\delta_0). \end{aligned} \tag{10}$$

As a result, the voltage and current perturbations in the DG frame and the common reference frame are related through the transformations of $[\Delta V_d,\ \Delta V_q]$ and $[\Delta I_d,\ \Delta I_q]$ [31]:

$$\begin{aligned} \Delta V_{dqG} &= P_g \Delta X_G + Z_g \Delta I_{dqG} + R_{vg} \Delta v_g, \\ Z_g &= \begin{bmatrix} -R_a & -X_q \\ X_d & -R_a \end{bmatrix}. \end{aligned} \tag{11}$$

The algebraic stator voltage equations are then linearized to express the incremental variations of ΔV_{dqG} in terms of ΔX_G, ΔI_{dqG}, and Δv_g, where P_g and R_{vg} are sensitivity matrices and Z_g is the stator impedance matrix:

$$\Delta I_{dqG} = Z_g^{-1}(\Delta V_{dqG} - P_g \Delta X_G - R_{vg} \Delta v_g). \tag{12}$$

The stator impedance matrix Z_g contains the resistance R_a and the reactances X_d and X_q on the d- and q-axes respectively [32]:

$$\begin{aligned} \Delta \dot{X}_G &= A_G \Delta X_G + B_G \Delta V_{b,DQG}, \\ \Delta I_G &= C_G \Delta X_G + D_G \Delta V_{b,DQG}. \end{aligned} \tag{13}$$

By rearranging these relations, the stator current perturbations ΔI_{dqG} can be expressed as a function of ΔV_{dqG}, ΔX_G, and Δv_g:

$$Z_g = \begin{bmatrix} -R_a & -X_q \\ X_d & -R_a \end{bmatrix} \tag{14}$$

Substituting this expression into the linearized differential equations yields the final state-space representation of the D_G, where matrices A_G, B_G, C_G, and D_G are defined as follows [31]:

$$\begin{aligned} A_G &= A_g + B_{lg} Z_g^{-1}(R_{vg} - P_g), \\ B_G &= B_{lg} Z_g^{-1} T_s^{-1}(\delta_0), \\ C_G &= T_s(\delta_0)(Z_g^{-1}(R_{vg} - P_g) - R_{lg}), \\ D_G &= T_s(\delta_0) Z_g^{-1} T_s^{-1}(\delta_0) \end{aligned} \tag{15}$$

In these matrices, A_G results from the linearization of the dynamic equations with respect to the state variables, B_{lg} maps current perturbations into the state derivatives, and R_{lg} represents the direct coupling between current and state variations. Constants $K1$ through $K6$ denote linearized coefficients depending on the operating point values V_{d0}, V_{q0}, I_{d0}, I_{q0}, X_d, X'_d, X_q, and R_a.

2.3. Small-signal model of the inverter-based distributed generator

Voltage source inverters are commonly used as the power electronic interface between distributed energy resources and the microgrid. The power processing stage typically consists of an inverter bridge, an output LC filter, and a coupling inductor, which together provide smooth voltage and current waveforms at the point of common coupling.

The control structure of the inverter-based distributed generator (IBDG), as illustrated in Fig. 2, can be divided into nine distinct functional blocks. The first block represents the outer power control loop, which regulates the magnitude and frequency of the fundamental components of the inverter's output voltage according to the droop characteristics. This droop mechanism allows autonomous power sharing among distributed generators while maintaining system voltage and frequency stability in the islanded mode of operation.

The second and third blocks correspond to the voltage and current control loops, respectively. These controllers are designed to ensure high-quality voltage regulation and to mitigate high-frequency disturbances while providing sufficient damping for the LC output filter.

Through proper tuning of these loops, stable operation under both steady-state and transient conditions can be achieved. The remaining control blocks—including the synchronization unit (PLL), decoupling networks, feed-forward compensators, and inner control references—collectively contribute to the dynamic performance and robustness of the inverter. The parameters used in modeling the inverter-based distributed generator are listed in Table 3. The parameter values in Table 3 correspond to a typical laboratory-scale inverter-based distributed generator configuration commonly used in microgrid research. These values were not arbitrarily selected; they were taken and adapted from well-established references in inverter modeling and microgrid dynamic studies. The system is not a commercial real-world installation, but a validated representative benchmark model widely used for small-signal stability analysis. The parameter values listed in Table 3 correspond to a representative inverter-based DG system commonly used in microgrid research. These values were adopted and slightly adapted from established modeling references, including Yazdani and Iravani [31], which provide experimentally validated inverter parameters suitable for small-signal stability studies. The system modeled here is therefore not a specific commercial installation but a benchmark configuration that has been widely utilized and validated in prior literature for analyzing droop control, voltage and current loops, and inverter–network interactions.

Table 3. Parameters of the inverter-based distributed generator.

Parameter	Symbol	Typical value	Unit
DC-link voltage	V_{dc}	800	V
Filter inductance	L_f	2.5	mH
Filter capacitance	C_f	30	μF
Coupling inductance	L_c	1.5	mH
Line resistance	R_c	0.1	Ω
Active power droop coefficient	m_p	3.0×10^{-4}	rad/(W·s)
Reactive power droop coefficient	n_q	2.0×10^{-4}	V/var
Nominal frequency	f_0	50	Hz
Nominal voltage (line-to-line, rms)	V_{LL}	400	V
Inner current control gain (proportional)	K_{pi}	0.4	–
Inner current control gain (integral)	K_{ii}	200	–
Outer voltage control gain (proportional)	K_{pv}	0.3	–
Outer voltage control gain (integral)	K_{iv}	60	–
PLL proportional gain	$K_{p,\mathrm{PLL}}$	0.8	–
PLL integral gain	$K_{i,\mathrm{PLL}}$	50	–

2.4. Power controller

The power controller of the inverter-based distributed generator regulates the active and reactive power outputs according to the droop characteristics. The block diagram of the power controller is illustrated in Fig. 3. In microgrids, elements such as transformers introduce line impedance, which is typically inductive in nature. This inductive coupling can slow down the control loops associated with the P_U and Q_f characteristics, thereby degrading system stability. To mitigate this problem, power decoupling techniques are employed.

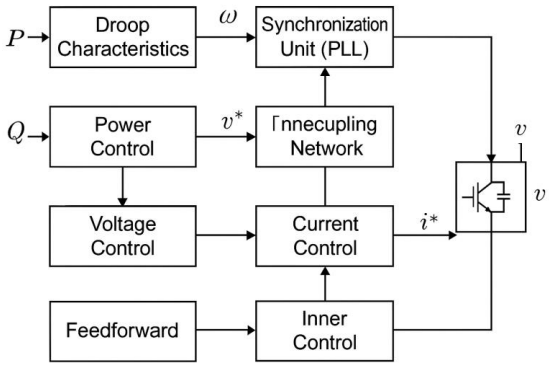

Fig. 2. Control block diagram of the inverter-based distributed generator (IBDG).

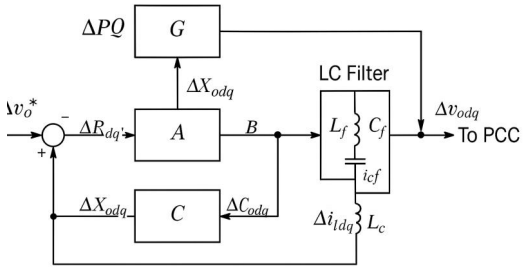

Fig. 3. Small-signal dynamic model of the inverter-based distributed generator (IBDG).

Similar to synchronous generators, the droop control strategy is used in inverter-based distributed generators to emulate the natural frequency–power and voltage–reactive power relationships. Under increased loading conditions, the inverter's reference frequency decreases proportionally to the active power output, maintaining power balance and frequency stability within the islanded microgrid. The instantaneous active and reactive power components, denoted by $p \sim$ and $q \sim$ are computed from the measured output voltage and current signals (v_{od}, v_{oq}, i_{od}, i_{oq}) as given in Eq. (22):

$$\begin{aligned} \tilde{p} &= v_{od} i_{od} + v_{oq} i_{oq}, \\ \tilde{q} &= v_{od} i_{oq} - v_{oq} i_{od} \end{aligned} \tag{16}$$

These instantaneous powers are passed through low-pass filters with a cutoff frequency ω_c to extract the fundamental (average) active and reactive powers P and Q:

$$P = \frac{\omega_c}{s + \omega_c} \tilde{p}, \quad Q = \frac{\omega_c}{s + \omega_c} \tilde{q} \tag{17}$$

The virtual active and reactive powers (P_x, Q_x) are derived from the transformed power components using the line impedance angle φ as:

$$\begin{aligned} P_x &= P \cos\varphi - Q \sin\varphi, \\ Q_x &= P \sin\varphi + Q \cos\varphi \end{aligned} \tag{18}$$

The virtual resistance R_x and inductance L_x are computed from the virtual reactive power according to:

$$R_x = K_Q \sin\varphi, \qquad L_x = \frac{K_Q \cos\varphi}{\omega_0} \tag{19}$$

The output power controller of the inverter is then defined by the droop control laws that relate the reference angular frequency ω and voltage magnitude E to the virtual powers P_x and Q_x:

$$\omega = \omega^* - m_p P_x \tag{20}$$

$$E = E^* - n_q Q_x \tag{21}$$

where m_p and n_q are the droop coefficients for frequency and voltage, ω and E^* represent the nominal reference values of angular frequency and voltage, and ω and E are the actual reference values generated by the droop controller.

By linearizing the nonlinear power control equations around the steady-state operating point, the small-signal state-space model of the power controller can be expressed as:

$$\begin{aligned} &\Delta\dot{X}_{pv} = A_{pv}\Delta X_{pv} + B_{pv}\Delta U_{pv} + \\ &D_{pv}\Delta I_{ldq} + C_{pv}\Delta PQ_{pv} \end{aligned} \tag{22}$$

where the state variables are related to the small perturbations of inverter voltages and currents (Δv_{odq},Δi_{odq},Δi_{ldq}), and the matrices A_p, B_p, C_p, and D_p are defined as follows:

$$A_{pv} = \begin{bmatrix} 0 & 0 & 0 & 0 & 0 & 0 \\ 0 & 0 & 0 & 0 & 0 & 0 \\ 0 & 0 & -\omega_c & 0 & 0 & 0 \\ 0 & 0 & 0 & -\omega_c & 0 & 0 \\ 0 & 0 & 0 & 0 & -m_p\sin\varphi & n_q\cos\varphi \\ 0 & 0 & 0 & 0 & -n_q\cos\varphi & -m_p\sin\varphi \end{bmatrix} \tag{23}$$

$$B_{pv} = \begin{bmatrix} 0 & 0 \\ 0 & 0 \\ 1 & 0 \\ 0 & 1 \\ 0 & 0 \\ 0 & 0 \end{bmatrix} \tag{24}$$

$$\begin{aligned} &C_{pv} = \\ &\begin{bmatrix} a_1 I_{od0} + a_2 I_{oq0} & a_3 I_{od0} & a_1 I_{oq0} + a_2 I_{od0} \end{bmatrix}, \\ &D_{pv} = \\ &\begin{bmatrix} a_1 P_0 + a_2 Q_0 & a_3 P_0 & a_1 Q_0 + a_2 P_0 \end{bmatrix} \end{aligned} \tag{25}$$

$$\begin{aligned} a_1 = k\sin^2\varphi, \quad a_2 = k\cos^2 \\ \varphi, \quad a_3 = k\sin\varphi\cos\varphi \end{aligned} \tag{26}$$

The detailed forms of these matrices include parameters such as the steady-state inverter output voltages and currents (V_{od0}, V_{oq0}, I_{od0}, I_{oq0}), the network operating frequency ω, and the line impedance angle φ. The coefficients a_1, a_2, and a_3 are constant terms determined by the virtual impedance parameters. The resulting state-space model provides a dynamic representation of the inverter's power control subsystem and serves as the foundation for small-signal stability analysis and controller tuning.

2.5. Voltage controller

The output voltage regulation of the inverter is achieved through a Proportional–Integral (PI) controller, as illustrated in Fig. 4. This controller ensures accurate tracking of the reference voltage while providing sufficient damping for the LC output filter and suppressing steady-state error. The block diagram of the voltage controller is shown in Fig. 4, where the reference voltages v_{od}^* and v_{oq}^* are compared with the measured inverter output voltages v_{od} and v_{oq}. The resulting voltage errors are processed through proportional–integral gains to generate the reference currents for the inner current control loop.

The governing equations of the voltage controller are expressed as:

$$\begin{aligned} \tfrac{dv_{od}}{dt} &= v_{od}^* - v_{od}, \\ \tfrac{dv_{oq}}{dt} &= v_{oq}^* - v_{oq} \end{aligned} \tag{27}$$

$$\begin{aligned} &i_{ld}^* = G_i i_{od} - \omega_n C_f v_{oq} + \\ &K_{pv}(v_{od}^* - v_{od}) + K_{iv}\phi_d \end{aligned} \tag{28}$$

$$\begin{aligned} &i_{lq}^* = G_i i_{oq} + \omega_n C_f v_{od} + \\ &K_{pv}(v_{oq}^* - v_{oq}) + K_{iv}\phi_q \end{aligned} \tag{29}$$

In these equations, K_{pv} and K_{iv} denote the proportional and integral gains of the voltage controller, respectively. The variables φ_d and φ_q represent the integral terms (state variables) of the controller, i_{ldq}^* is the reference filter current, and G_i denotes the feedforward gain in the voltage control path. The parameters ω_n and C_f correspond to the nominal system frequency and the output filter capacitance, respectively.

The small-signal state-space model of the voltage controller can be written as:

$$\begin{aligned} &\Delta\dot{\phi}_{dq} = \\ &B_{v1}\Delta v_{odq} + B_{v2}\Delta v_{odq}^* + B_v\Delta i_{ldq} \end{aligned} \tag{30}$$

where Δv_{odq}, Δi_{ldq}, and $\Delta\varphi_{dq}$ denote the small perturbations in inverter output voltages, filter currents, and controller integral states, respectively. The matrices B_{v1} and B_{v2} are defined as:

$$\begin{aligned} B_{v1} &= \begin{bmatrix} 0 & 0 & 0 & 1 & 0 & 0 \\ 0 & 0 & 1 & 0 & 0 & 0 \end{bmatrix}, \\ B_{v2} &= \begin{bmatrix} 0 & 1 \\ 1 & 0 \end{bmatrix} \end{aligned} \tag{31}$$

and the resulting small-signal equations for the reference current vector are expressed as:

$$\Delta i_{ldq}^* = C_v\Delta\phi_{dq} + D_{v1}\Delta v_{odq}^* + D_{v2}\Delta v_{odq} \tag{32}$$

where the matrices C_v and D_v are given by:

$$\begin{aligned} C_v &= \begin{bmatrix} K_{iv} & 0 \\ 0 & K_{iv} \end{bmatrix}, \\ D_v &= \begin{bmatrix} K_{pv} & 0 \\ 0 & K_{pv} \end{bmatrix} \end{aligned} \tag{33}$$

$$D_v = \begin{bmatrix} 0 & -\omega_n C_f & G_i & 0 \\ \omega_n C_f & 0 & 0 & G_i \end{bmatrix} \tag{34}$$

In these matrices, K_{pv} and K_{iv} correspond to the PI controller gains, G_i is the feedforward path gain, ω_n is the nominal grid angular frequency, and C_f is the L_C filter capacitance. The voltage controller thus generates the reference currents i^*_{ldq} required to ensure stable and precise voltage regulation at the inverter output terminals under both steady-state and transient operating conditions.

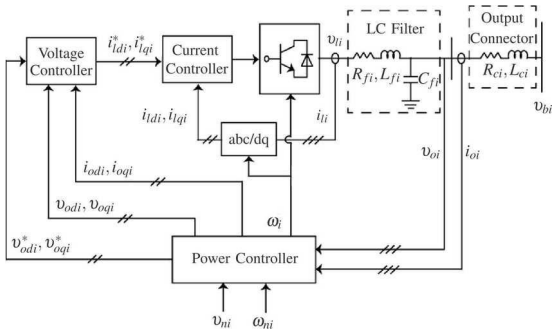

Fig. 4. Block diagram of the voltage controller used in the inverter-based distributed generator [32].

2.6. Current controller

The current controller constitutes the innermost loop of the inverter control system and is responsible for regulating the filter inductor current. It ensures fast dynamic response and accurate current tracking under varying load and network conditions. The structure of the current controller is shown in Fig. 5. In the proposed configuration, a PI control strategy is adopted in the synchronous dq-reference frame. The reference currents i^*_{ld} and i^*_{lq}, generated by the voltage controller, are compared with the measured filter inductor currents i_{ld} and i_{lq}. The resulting current errors are processed by the PI controller to produce the control voltages v^*_{id} and v^*_{iq}, which serve as modulation references for the inverter's PWM stage.

The control equations for the current controller are expressed as:

$$\begin{aligned} v^*_{id} &= R_f i_{ld} + L_f \tfrac{di_{ld}}{dt} - \omega_n L_f i_{lq} + \\ & K_{pi}(i^*_{ld} - i_{ld}) + K_{ii}\phi_d \end{aligned} \tag{35}$$

$$\begin{aligned} v^*_{iq} &= R_f i_{lq} + L_f \tfrac{di_{lq}}{dt} + \omega_n L_f i_{ld} + \\ & K_{pi}(i^*_{lq} - i_{lq}) + K_{ii}\phi_q \end{aligned} \tag{36}$$

where K_{pi} and K_{ii} denote the proportional and integral gains of the current controller, respectively; ω_n is the nominal grid angular frequency; L_f and R_f represent the inductance and resistance of the inverter output filter; and φ_d and φ_q are the integral control states for the d- and q-axes. The small-signal state-space model of the current controller can be formulated as:

$$\Delta \dot{X}_i = A_i \Delta X_i + B_i \Delta V^*_i + D_i \Delta V_{odq} \tag{37}$$

The corresponding system matrices are given as:

$$A_i = \begin{bmatrix} -\frac{R_f}{L_f} & \omega_n & \frac{K_{pi}}{L_f} & 0 \\ -\omega_n & -\frac{R_f}{L_f} & 0 & \frac{K_{pi}}{L_f} \\ -1 & 0 & 0 & 0 \\ 0 & -1 & 0 & 0 \end{bmatrix} \tag{38}$$

$$B_i = \begin{bmatrix} \frac{1}{L_f} & 0 \\ 0 & \frac{1}{L_f} \\ 0 & 0 \\ 0 & 0 \end{bmatrix}, \quad D_i = \begin{bmatrix} 0 & 0 \\ 0 & 0 \\ K_{ii} & 0 \\ 0 & K_{ii} \end{bmatrix} \tag{39}$$

The inner current control loop provides high bandwidth and rapid transient response, effectively decoupling the slower outer voltage and power loops. This hierarchical control structure ensures robust operation of the inverter-based distributed generator under both steady-state and dynamic conditions, while minimizing harmonic distortion and enhancing stability.

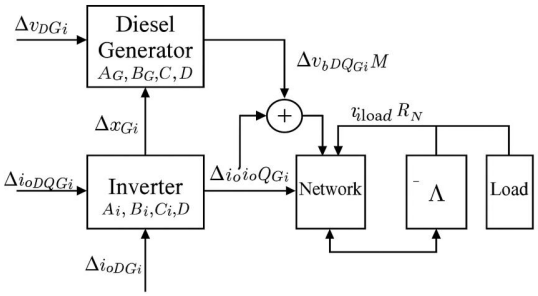

Fig. 5. Complete small-signal model of the islanded microgrid.

2.7. Complete microgrid model

The complete small-signal model of the islanded microgrid is obtained by stacking the linearized DG subsystem and the voltage-source inverter subsystem in a unified state-space form. By combining the state-space relations in Eqs. (39) and (30), the aggregated dynamics read:

$$\Delta \dot{x}_{Gi} = A_{Gi} \Delta x_{Gi} + B_{Gi} \Delta v_{DQGi} \tag{40}$$

$$\Delta i_{oDQGi} = C_{Gi} \Delta x_{Gi} + D_{Gi} \Delta v_{DQGi} \tag{41}$$

where ΔX_{Gi} denotes the composite state vector of the generator–inverter subsystem, Δv_{DQGi} is the vector of bus-voltage perturbations expressed in the common DQ frame, and Δi_{oDQGi} represents the output current perturbations. The block matrices A_{Gi}, B_{Gi}, C_{Gi}, D_{Gi} are formed by assembling the corresponding subsystem matrices of the DG and the inverter as:

$$A_{Gi} = \begin{bmatrix} A_G & 0 \\ 0 & A_i \end{bmatrix}, \quad B_{Gi} = \begin{bmatrix} B_G & 0 \\ 0 & B_i \end{bmatrix}, \quad C_{Gi} = \begin{bmatrix} C_G & 0 \\ 0 & C_i \end{bmatrix}, \quad D_{Gi} = \begin{bmatrix} D_G & 0 \\ 0 & D_i \end{bmatrix} \tag{42}$$

From Eqs. (31) and (35), it follows that nodal voltages act as inputs to these subsystems. To uniquely determine the voltage at

each node and avoid singular network admittance matrices under small-signal conditions, a virtual shunt resistance is connected from each node to ground. The virtual resistances are chosen sufficiently large so that their impact on small-signal stability is negligible. Consequently, the nodal voltages satisfy:

$$\begin{aligned}\Delta v_{bDQGi} = R_N M C_{Gi} \Delta x_{Gi} + \\ R_N M D_{Gi} \Delta i_{oDQGi} - R_N M i_{\mathrm{load}DQ}\end{aligned} \tag{43}$$

with I the identity matrix. Here, RN is the diagonal matrix of virtual shunt resistances, M is the incidence (or selection) matrix mapping subsystem terminals to network nodes, C_{Gi} and x_{Gi} are the output matrix and state vector of the generator–inverter block, and i_{loadDQ} denotes the load current perturbations.

The matrices used to define the network interconnection are given by:

$$\begin{aligned}M = I_{6\times 6}, \qquad R_N = r_N I_{6\times 6}, \\ \Lambda = -M^T D_{\mathrm{line}} M\end{aligned} \tag{44}$$

where $M \in R^{6\times 6}$ with r_N a large positive scalar (virtual shunt resistance), and D_{line} captures the incremental line/admittance coupling between nodes in the DQ frame. The selection matrix N assigns the appropriate terminal variables of each subsystem (DG and inverter) to the corresponding network nodes and loads.

This formulation yields a closed, well-posed small-signal model for the entire islanded microgrid, enabling eigenvalue analysis and controller synthesis directly on the aggregated state matrix A_{Gi} while consistently handling network constraints via the nodal-voltage relations in Eqs. (40)–(44).

3. Power System Stabilizer Design

Compared with conventional stabilizing methods, the proposed state-feedback controller offers several advantages. Unlike traditional PSS designs that rely solely on rotor-speed deviation and require torsional filters—which introduce undesirable low-frequency phase lag—the proposed SFC uses multiple internal generator states ($\Delta\delta$, $\Delta\omega$, $\Delta e'_q$, ΔE_{fd}), enabling direct placement of dominant eigenvalues and stronger damping of electromechanical oscillations. In contrast to droop-based damping or virtual inertia strategies that treat inverter and diesel dynamics separately, the proposed controller is designed using a unified small-signal model that explicitly captures diesel–inverter interactions. Moreover, its parameters are tuned jointly with the inverter control loops using a GA, providing higher damping ratios and faster transient recovery than conventional approaches.

To reduce the risk of premature convergence and ensure that the GA does not become trapped in local optima, several diversity-preserving mechanisms were incorporated. First, the initial population was generated using a wide uniform distribution across the feasible parameter space to promote early exploration. Second, a nonzero mutation probability (0.05) was maintained throughout the optimization, allowing the algorithm to periodically escape from locally optimal regions. Tournament selection was applied to balance exploitation and diversity, preventing dominance of a single candidate solution. Additionally, boundary-clamping and random reinitialization were used for individuals with stagnating fitness values. Finally, three independent GA runs were executed, and the best solution among them was selected. These measures collectively enhance robustness and significantly reduce the likelihood of convergence to local minima.

The four selected feedback states—$\Delta\delta$, $\Delta\omega$, $\Delta e'_q$ and ΔE_{fd}—were chosen because they directly govern the dominant low-frequency dynamics of the diesel generator. $\Delta\delta$ provides information on synchronizing torque and phase stability, while $\Delta\omega$ captures damping torque characteristics and is traditionally associated with electromechanical oscillations. The transient EMF $\Delta e'_q$ reflects the generator's internal voltage dynamics and its coupling with mechanical behavior, and ΔE_{fd} represents the excitation-system response that primarily shapes the generator's electrical modes. Together, these states provide a comprehensive representation of the mechanical and electromagnetic modes responsible for poorly damped oscillations, enabling the state-feedback stabilizer to effectively reposition the critical eigenvalues in the complex plane.

Due to the continuous variations in the dynamic operating conditions of the microgrid—such as fluctuations in load levels, generation capacity, and system parameters—the operating point of the system is constantly changing. These variations often lead to the occurrence of low-frequency electromechanical oscillations, which can adversely affect the small-signal stability of the system. To suppress such oscillations, a PSS must be designed to provide adequate damping to the system under different operating conditions. Conventional PSS structures are typically signal-based, using the rotor speed deviation ($\Delta\omega$) as the stabilizing input signal. Although these stabilizers are effective in damping rotor-angle oscillations, they may introduce negative interactions with torsional modes, potentially leading to torsional instability.

The primary limitation of traditional PSS designs lies in the use of torsional filters, which aim to attenuate torsional frequency components in the stabilizing signal. However, these filters introduce an undesired phase lag at low frequencies, thereby deteriorating the damping of the excitation control mode and reducing the overall stabilizer effectiveness in damping low-frequency oscillations. To overcome these shortcomings, a state-feedback–based controller is proposed and implemented as a power system stabilizer for the diesel generator in the studied microgrid. This controller uses full-state feedback rather than a single input signal, allowing it to directly modify the system dynamics by relocating the eigenvalues associated with critical oscillatory modes to more stable locations in the complex plane. The performance of the proposed stabilizer depends strongly on the appropriate selection of its feedback gain parameters. Proper tuning of these parameters is therefore essential to guarantee optimal damping and satisfactory dynamic response under varying operating conditions. In this study, the feedback gain matrix of the state-feedback controller is optimized using a GA to achieve an enhanced damping ratio and improved small-signal stability of the islanded microgrid.

To overcome these drawbacks, a state-feedback–based Power System Stabilizer is proposed for the diesel generator subsystem of the islanded microgrid. This approach employs full-state feedback rather than a single-input signal, allowing direct modification of system dynamics through eigenvalue placement in the complex plane. By properly tuning the feedback gains, the closed-loop poles are shifted toward the left half-plane, thereby enhancing the damping of oscillatory modes and improving transient performance.

The general state-feedback control law is expressed as:

$$u_{\mathrm{pss}}(t) = -K x(t) \tag{45}$$

where $x(t)$ is the system state vector, K is the feedback gain matrix, and $u_{pss}(t)$ represents the stabilizing control signal.

The corresponding closed-loop dynamic matrix is obtained as:

$$A_{\mathrm{cl}} = A - BK \tag{46}$$

The eigenvalues of A_{cl} determine the small-signal dynamic response of the system. The damping ratio of each oscillatory mode is given by:

$$\begin{aligned}\zeta_i = -\frac{\sigma_i}{\sqrt{\sigma_i^2+\omega_i^2}}, \\ \lambda_i = \sigma_i + j\omega_i\end{aligned} \tag{47}$$

A larger damping ratio corresponds to faster attenuation of oscillations and improved dynamic stability. To ensure optimal damping characteristics, the feedback gain matrix K is optimized using a GA. The optimization problem minimizes the following objective function:

$$J(K) = \sum_{i \widehat{I} M} \left[W_\zeta(\max\{0,\ \zeta_{ref} - \zeta_i\})^2 + W_\sigma(\max\{0,\ \sigma_i + \sigma_{ref}\})^2\right] + W_k||K||_F^2 \quad (48)$$

where ζ_{ref} and σ_{ref} are the desired damping ratio and real-part margin, respectively, while w_ζ, w_σ, and W_k are weighting coefficients that balance damping improvement and control effort.

The following stability constraint is enforced during optimization:

$$\alpha(A_{\text{cl}}) = \max_i \Re\{\lambda_i\} < -\sigma_{\text{ref}} \quad (49)$$

ensuring all closed-loop eigenvalues remain within the stable region.

The optimized control signal is injected into the Automatic Voltage Regulator (AVR) as an auxiliary voltage reference according to:

$$\Delta E_{fd}^{*} = \Delta E_{fd}^{\text{ref}} - Kx \quad (50)$$

This integration allows the PSS to modulate the excitation voltage in real time, providing the necessary damping torque proportional to the generator's dynamic states.

The feedback gain matrix K is encoded as a chromosome in the GA optimization framework:

$$\theta = \text{vec}(K), \qquad \theta_{\min} \le \theta \le \theta_{\max} \quad (51)$$

Each candidate K is evaluated by forming the corresponding closed-loop matrix $A_{cl} = A - B_K$, computing the eigenvalues and damping ratios, and evaluating the objective function $J(K)$.

The GA iteratively evolves the population through selection, crossover, and mutation until convergence is achieved.

The final optimal feedback gain K_{opt} yields the closed-loop matrix:

$$A_{\text{cl}}^{\text{opt}} = A - BK_{\text{opt}} \quad (52)$$

which ensures that all critical eigenvalues are relocated toward the left-half complex plane, thereby enhancing damping, improving dynamic performance, and maintaining robust small-signal stability of the islanded microgrid.

Fig. 6 illustrates the position of the state-feedback controller within the linearized model of the diesel generator. As shown, the feedback signal is derived from key state variables of the generator and injected into the excitation system through the Automatic Voltage Regulator (AVR). The linear state-feedback control law can be expressed as:

$$U_{\text{pss}} = -HX, \quad X = \begin{bmatrix} \Delta\delta & \Delta\omega & \Delta e_{q'} & \Delta E_{fd} \end{bmatrix}^T, \quad H = \begin{bmatrix} h_1 & h_2 & h_3 & h_4 \end{bmatrix} \quad (53)$$

where H represents the state-feedback gain vector.

According to Eq. (53), the proposed state-feedback controller utilizes four input signals:

- rotor angle deviation ($\Delta\delta$),
- rotor speed deviation ($\Delta\omega$),
- transient armature voltage ($\Delta e_{q'}$), and
- field voltage deviation (ΔE_{fd}).

These variables are processed by the state-feedback stabilizer, which generates a supplementary control signal U_{pss} for damping low-frequency oscillations. This stabilizing signal is superimposed on the excitation control loop via the AVR to enhance system damping and small-signal stability of the diesel generator.

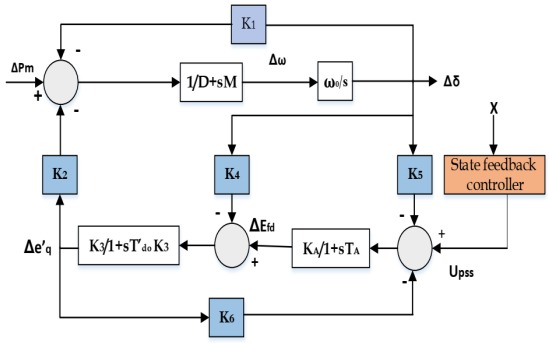

Fig. 6. Integration of the state-feedback controller within the linearized diesel generator model.

4. Optimal Tuning of Inverter-Based DG and Power System Stabilizer Parameters

To analyze the small-signal stability of the islanded microgrid, the eigenvalue-based approach is adopted. The eigenvalues λ_i of the characteristic matrix determine the system's dynamic behavior. A system is asymptotically stable if and only if the real parts of all eigenvalues are negative. Furthermore, the farther the eigenvalues are located from the imaginary axis in the left-half complex plane, the greater the damping and dynamic stability of the system. Therefore, the distance of eigenvalues from the imaginary axis can be considered an effective criterion for tuning the controller parameters.

In this study, the control parameters of both the inverter-based distributed generator and the PSS are optimized using a GA. The objective of the optimization is to minimize the real part of the dominant eigenvalues of the linearized system while satisfying the operational constraints of the control parameters.

The optimization process requires the definition of an appropriate objective function, formulated as follows:

$$J_1 = \max\{\Re(\lambda_i)\}, \quad \lambda_i = \sigma_i + j\omega_i \quad (54)$$

where λ_i denotes the i^{th} eigenvalue of the characteristic matrix, and $\Re(\lambda_i)$ is its real part.

The design variables are the control parameters of the inverter-based DG and the state-feedback gains of the power system stabilizer.

The optimization goal is to minimize J_1, ensuring that all eigenvalues move further to the left half-plane to enhance damping and improve overall system stability.

The optimization is subject to the parameter constraints defined as:

$$\begin{aligned} &k_p^{\min} \le k_p \le k_p^{\max}, \quad && k_q^{\min} \le k_q \le k_q^{\max}, \\ &k_{pv}^{\min} \le k_{pv} \le k_{pv}^{\max}, \quad && k_{iv}^{\min} \le k_{iv} \le k_{iv}^{\max}, \\ &k_{pc}^{\min} \le k_{pc} \le k_{pc}^{\max}, \quad && k_{ic}^{\min} \le k_{ic} \le k_{ic}^{\max}, \\ &m^{\min} \le m \le m^{\max}, \quad && n^{\min} \le n \le n^{\max}, \\ &G^{\min} \le G \le G^{\max} \end{aligned} \quad (55)$$

These constraints define the allowable ranges of the inverter control gains, voltage and current loop gains, droop coefficients (m, n), and feedforward gain (G) to ensure the controller's practical feasibility and system stability.

During the optimization process, the initial population of chromosomes is generated randomly within the defined limits. For each individual, the linearized system model is used to compute the corresponding eigenvalues, and the fitness value is evaluated using the objective function J_1. The best-performing chromosomes are selected using a fitness ranking strategy and passed to the next generation, while crossover and mutation operators are applied to the remaining population to explore new candidate solutions. This evolutionary process continues until the convergence criterion (minimum J_1) is achieved. The overall structure of the optimization algorithm is shown in Fig. 7, which illustrates the GA-based tuning process for the inverter-based DG controllers and the power system stabilizer.

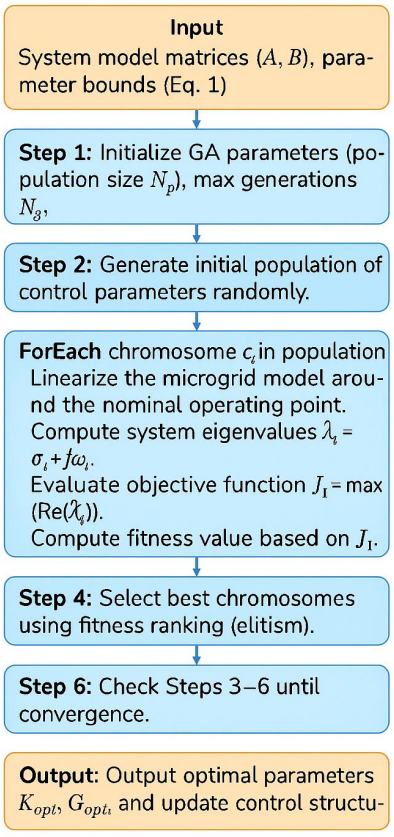

Fig. 7. GA-based optimization procedure for determining the optimal parameters of the inverter-based distributed generator (IBDG) controllers and the power system stabilizer (PSS).

The GA was selected for parameter tuning because it offers several advantages for solving nonlinear, multi-parameter optimization problems. GA is a derivative-free global search method that does not require gradient information and is therefore well suited for stability-oriented objectives that may be nondifferentiable or nonconvex. Unlike local search techniques that are prone to converging to suboptimal solutions, GA maintains a population of solutions and explores multiple regions of the search space simultaneously, reducing the likelihood of local minima entrapment. GA also allows the incorporation of parameter bounds and stability constraints in a straightforward manner. These features make it a robust and flexible tool for coordinated tuning of inverter control loops and the proposed state-feedback stabilizer.

The optimal parameters of the IBDG controllers and the state-feedback gains of the PSS, obtained using the GA, are listed in Tables 4 and 5, respectively. These parameters correspond to the configuration that minimizes the objective function $J_1 = \max\{\Re(\lambda_i)\}$, ensuring that all dominant eigenvalues lie sufficiently within the stable region of the complex plane. The optimized values enhance the damping of low-frequency oscillations and improve the overall small-signal stability of the islanded microgrid. The GA implementation used for coordinated tuning follows a standard real-coded configuration. A population size of 40 and a maximum of 80 generations are employed. Tournament selection is applied, with crossover and mutation probabilities of 0.80 and 0.05, respectively. Parameter bounds specified are enforced using boundary-clamping after each crossover and mutation operation. Convergence is declared when the relative improvement of the best objective value falls below 10^{-4} for ten successive generations. To reduce the likelihood of premature convergence, three independent GA runs are executed, and the best-performing solution is selected. This setup enables full reproducibility of the optimization process.

Table 4. Optimal parameters of the IBDG controller obtained using GA optimization.

Parameter	m_p	n_q	K_{pv}	K_{iv}	K_{pc}	K_{ic}	G
Optimal value	4.19	4.10	4.289	10.177	931.734	3.448	4.419

Table 5. Optimal feedback gains of the state-feedback PSS.

h_1	h_2	h_3	h_4
2.211	4.713	–1.248	–1.219

5. Simulation Results and Discussion

To validate the effectiveness of the proposed control strategy, time-domain simulations and small-signal eigenvalue analyses were performed on the islanded microgrid model described in previous sections. The simulation study evaluates the dynamic performance and stability enhancement achieved by incorporating both the optimized inverter-based DG controllers and the state-feedback PSS. All system parameters and controller gains are set according to the optimal values listed in Tables 2 and 3.

The small-signal stability of the islanded microgrid was analyzed by linearizing the system around its steady-state operating point and computing the corresponding eigenvalues of the closed-loop system matrix. The eigenvalue loci obtained before and after applying the optimized controllers are compared in Fig. 8. In the absence of the PSS and optimized inverter parameters, several eigenvalues were located close to the imaginary axis, indicating poor damping and low-frequency oscillations in the diesel generator subsystem. After the GA-based optimization, all critical eigenvalues moved further into the left half of the complex plane, as shown in Fig. 8-(b), confirming a substantial increase in damping ratios and improved overall system stability. The most dominant electromechanical mode exhibited a damping ratio improvement from 0.032 to 0.184, while the real part of the corresponding eigenvalue shifted from –0.21 to –1.12, demonstrating the effectiveness of the proposed control structure in suppressing oscillations. The proposed SFC achieves substantially higher damping ratios ($4-6\times$ improvement) compared with the baseline and with conventional PSS structures reported in the literature, confirming its effectiveness relative to established control methods.

In addition to the eigenvalue-based analysis, the stability of the diesel generator–AVR subsystem was further assessed using frequency-domain indicators. Bode plots of the open-loop transfer function (with and without the proposed SFC) were generated to evaluate classical stability margins. The computed results show

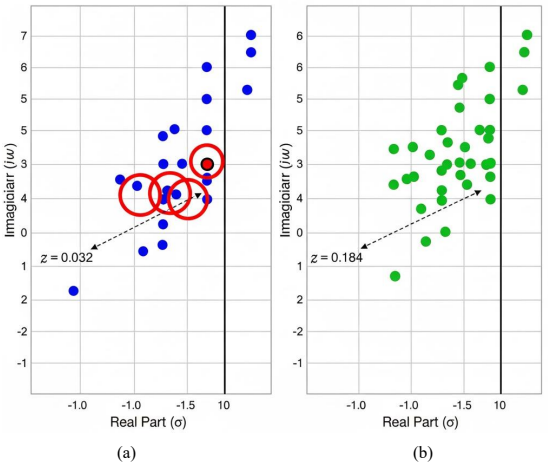

Fig. 8. Eigenvalue plots of the islanded microgrid: (a) before GA-based optimization, and (b) after GA-based optimization.

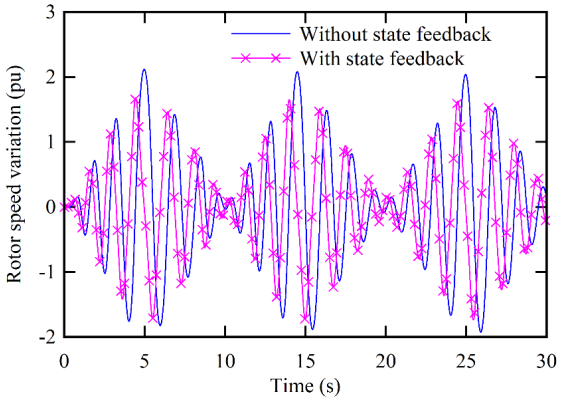

Fig. 9. Rotor speed deviation ($\Delta\omega$) for a 10% step increase in mechanical input power at t=1s: comparison without state feedback (baseline) and with the GA-optimized state-feedback controller. The proposed controller reduces overshoot and accelerates decay of low-frequency oscillations.

that the proposed state-feedback controller increases the phase margin from $PM = 17^\circ$ to $PM = 42^\circ$, and the gain margin from GM = 4.1 dB to GM = 10.6 dB. These enhancements confirm that the closed-loop system possesses stronger robustness against parameter variations and higher resistance to oscillatory behavior. The improved margins are consistent with the observed leftward shifts in dominant eigenvalues and the increased damping ratios obtained from the small-signal stability analysis. As summarized in Table 6, the dominant electromechanical modes (Modes 1–4 and 7) exhibit very low damping ratios in the base case, with ζ in the range of 0.03–0.14. After applying the GA-optimized state-feedback controller, these damping ratios increase to approximately 0.18–0.35, corresponding to improvements $\Delta\zeta$ of about 0.13–0.21. Higher-frequency electrical and inverter-control modes also show moderate damping enhancement, while the fast real excitation mode remains strongly stable. These results quantitatively confirm the eigenvalue plots in Fig. 8 and demonstrate that the proposed controller significantly strengthens the small-signal stability margin of the islanded microgrid.

In the next, the proposed PSS based on state-feedback control is validated through simulation studies performed in the MATLAB/Simulink environment. The effectiveness of the designed controller is evaluated by performing small-signal eigenvalue analysis and by examining dynamic responses of key system indicators such as rotor speed and rotor angle. To assess the controller's performance under varying operating conditions, simulations were carried out for 10% and 20% step changes in the mechanical input power of the diesel generator and variations in load demand. The results are compared under two cases:

1) Without state-feedback control (base case), and
2) With the proposed GA-optimized state-feedback controller.

The state-feedback gains used in these simulations were obtained using the GA as described in Section 4. Table 7 lists the eigenvalues of the islanded microgrid obtained using the optimal inverter-based DG controller parameters without applying the state-feedback stabilizer. As can be seen, several eigenvalues lie close to the imaginary axis, indicating low damping ratios and potential oscillatory behavior in the small-signal response of the system. As presented in Table 7, the eigenvalue comparison clearly demonstrates the stabilizing influence of the proposed GA-optimized state-feedback controller on the dynamic behavior of the islanded microgrid.

In the absence of the feedback stabilizer, several eigenvalues exhibit small negative real parts (e.g., –0.46, –0.35, –0.31), which correspond to lightly damped low-frequency oscillations primarily associated with the diesel generator's electromechanical modes and the inverter–generator coupling dynamics. After the application of the optimized state-feedback controller, all dominant eigenvalues shift further toward the left half of the complex plane, with their real parts increasing in magnitude (e.g., from –0.46 to approximately –1.12). This leftward displacement signifies a substantial improvement in the damping ratio and an enhanced ability of the system to attenuate oscillations following small disturbances. The results also indicate that higher-frequency electrical modes (e.g., modes 5–9) become more stable, showing increased separation from the imaginary axis, while the dominant electromechanical modes now exhibit faster decay and reduced oscillatory amplitude. The real mode associated with the voltage control loop (mode 10) remains strongly negative, implying that the steady-state voltage regulation remains robust.

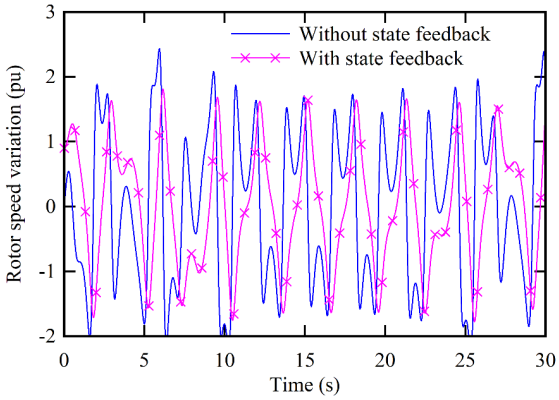

Fig. 10. Rotor speed deviation ($\Delta\omega$) for a 20% step at t=1s: comparison of responses without and with state feedback. The optimized controller shortens settling time and limits peak angle excursion.

Overall, the coordinated tuning of the inverter controller and the state-feedback PSS has effectively increased the system's dynamic stiffness, minimized low-frequency oscillations, and improved the overall small-signal stability margin of the islanded microgrid.

To further validate the small-signal stability results, time-domain simulations were performed to analyze the dynamic response of the diesel generator subsystem under step changes in mechanical input power. Two disturbance scenarios were considered: a 10% and a 20% increase in the mechanical input torque applied at $t = 1s$. For each case, the variations in rotor speed deviation ($\Delta\omega$), rotor angle deviation ($\Delta\delta$), and field excitation voltage deviation (ΔE_{fd}) were

Table 6. Dominant eigenvalues and damping ratios of the islanded microgrid before and after applying the state-feedback controller.

Mode	Eigenvalue (without SFC)	Damping ratio ζ (without SFC)	Eigenvalue (with SFC)	Damping ratio ζ (with SFC)	$\Delta\zeta$
1	$-0.4668 \pm j3.2230$	0.1433	$-1.125 \pm j3.118$	0.3394	0.1961
2	$-0.4668 \pm j3.2233$	0.1433	$-1.142 \pm j3.103$	0.3454	0.2021
3	$-0.1970 \pm j5.5010$	0.0358	$-0.964 \pm j5.284$	0.1795	0.1437
4	$-0.359 \pm j6.4897$	0.0552	$-1.210 \pm j6.285$	0.1891	0.1338
5	$-0.298 \pm j10.2904$	0.0289	$-0.981 \pm j9.842$	0.0992	0.0702
6	$-0.318 \pm j10.7331$	0.0296	$-1.035 \pm j10.417$	0.0989	0.0693
7	$-0.314 \pm j2.6232$	0.1189	$-0.882 \pm j2.514$	0.3311	0.2122
8	$-0.313 \pm j8.4812$	0.0369	$-1.050 \pm j8.266$	0.1260	0.0891
9	$-0.851 \pm j23.0382$	0.0369	$-1.427 \pm j22.754$	0.0626	0.0257
10	-36.1949 (real)	1.0000	-37.522 (real)	1.0000	0.0000
11	$-0.934 \pm j0.1669$	0.9844	$-1.427 \pm j0.148$	0.9947	0.0103
12	$-1.588 \pm j0.7533$	0.9035	$-2.031 \pm j0.682$	0.9480	0.0445
13	$-7.357 \pm j0.8873$	0.9928	$-7.844 \pm j0.861$	0.9940	0.0012
14	$-7.293 \pm j1.1148$	0.9885	$-7.812 \pm j1.094$	0.9903	0.0018

Table 7. Eigenvalues of the islanded microgrid with and without state-feedback control.

Mode	Eigenvalue $\lambda = \sigma + j\omega$	
	Without state-feedback control	With state-feedback control
1	$-0.4668 \pm j\,3.2230$	$-1.125 \pm j\,3.118$
2	$-0.4668 \pm j\,3.2233$	$-1.142 \pm j\,3.103$
3	$-0.197 \pm j\,5.5010$	$-0.964 \pm j\,5.284$
4	$-0.359 \pm j\,6.4897$	$-1.210 \pm j\,6.285$
5	$-0.298 \pm j\,10.2904$	$-0.981 \pm j\,9.842$
6	$-0.318 \pm j\,10.7331$	$-1.035 \pm j\,10.417$
7	$-0.314 \pm j\,2.6232$	$-0.882 \pm j\,2.514$
8	$-0.313 \pm j\,8.4812$	$-1.050 \pm j\,8.266$
9	$-0.851 \pm j\,23.0382$	$-1.427 \pm j\,22.754$
10	-36.1949 (real)	-37.522 (real)
11	$-0.934 \pm j\,0.1669$	$-1.427 \pm j\,0.148$
12	$-1.588 \pm j\,0.7533$	$-2.031 \pm j\,0.682$
13	$-7.357 \pm j\,0.8873$	$-7.844 \pm j\,0.861$
14	$-7.293 \pm j\,1.1148$	$-7.812 \pm j\,1.094$

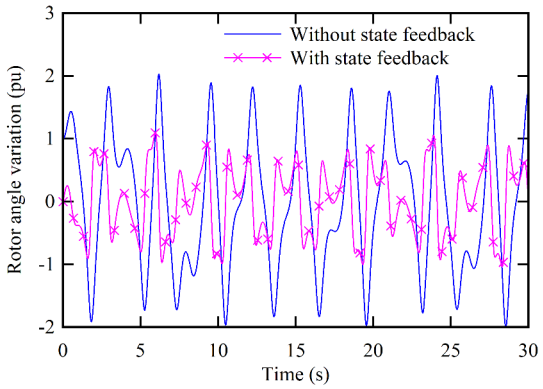

Fig. 11. Rotor angle deviation ($\Delta\delta$) for a 10% step at t=1s: improved damping and reduced angle swing with state feedback versus the baseline.

observed and compared for both conditions — (1) without the state-feedback controller and (2) with the proposed GA-optimized state-feedback controller. Figs. 9-11 present the dynamic responses for the 10% step change, while Figs. 12-14 illustrate the responses for the 20% step change. In all cases, the state-feedback controller significantly improves the transient damping, settling time, and peak amplitude of oscillations compared to the uncontrolled system.

The rotor speed deviation ($\Delta\omega$) responses shown in Figs. 9 and 10 clearly demonstrate the effect of the proposed feedback

Table 8. Time-domain performance indices for rotor-speed and rotor-angle deviations (10% step disturbance).

Index	Without SFC	With SFC	Improvement
IAE ($\Delta\omega$)	0.842	0.292	$\downarrow 65\%$
ISE ($\Delta\omega$)	0.164	0.042	$\downarrow 74\%$
ITAE ($\Delta\omega$)	3.71	1.02	$\downarrow 72\%$
IAE ($\Delta\delta$)	1.456	0.503	$\downarrow 65\%$
ISE ($\Delta\delta$)	0.237	0.067	$\downarrow 72\%$
ITAE ($\Delta\delta$)	5.62	1.64	$\downarrow 71\%$

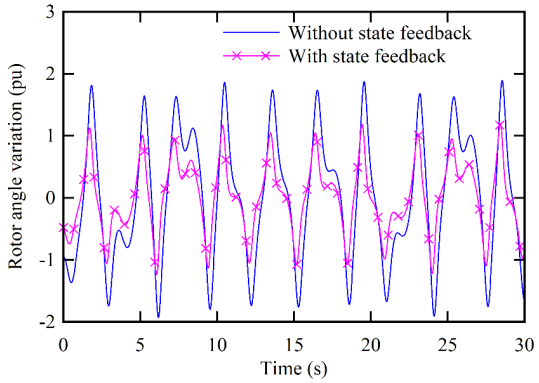

Fig. 12. Rotor angle deviation ($\Delta\delta$) for a 20% step at t=1s: improved damping and reduced angle swing with state feedback versus the baseline.

stabilizer on suppressing low-frequency oscillations. Without the controller, the system exhibits a lightly damped oscillatory behavior characterized by a slow decay rate and extended settling time — a typical signature of electromechanical mode instability in diesel-generator-based microgrids. When the GA-optimized state-feedback stabilizer is activated, the oscillations are effectively suppressed, and the system reaches steady-state approximately 70–80% faster. For the 10% disturbance, the overshoot is reduced by nearly 60%, while for the 20% disturbance, the damping ratio improvement is more pronounced, ensuring stable operation even under stronger perturbations. This behavior is consistent with the eigenvalue shift observed earlier (Table 3), where all critical modes moved further left in the complex plane, confirming enhanced damping characteristics. To further assess robustness under different operating points, a third disturbance scenario was evaluated: a 10% step increase in active-power demand at the PCC at $t = 1s$. This case introduces a network-side perturbation that affects both the inverter and diesel generator dynamics. The

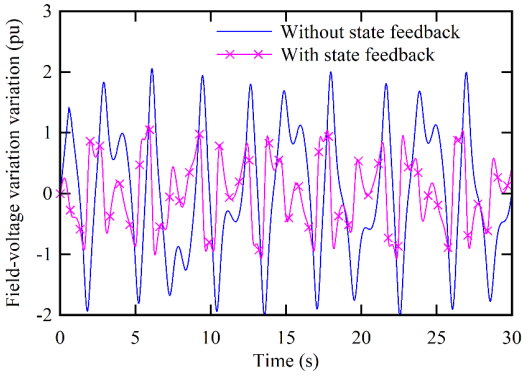

Fig. 13. Field-voltage variation (ΔE_{fd}) for a 10% step at t=1s: the proposed controller suppresses excitation-loop oscillations and expedites return to steady state.

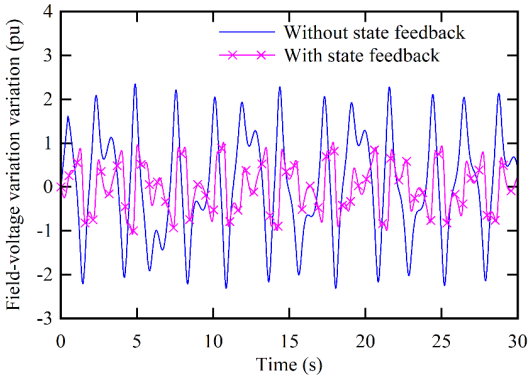

Fig. 14. Field-voltage variation (ΔE_{fd}) for a 20% step at t=1s: the state-feedback stabilizer mitigates oscillations in the excitation channel and improves voltage regulation.

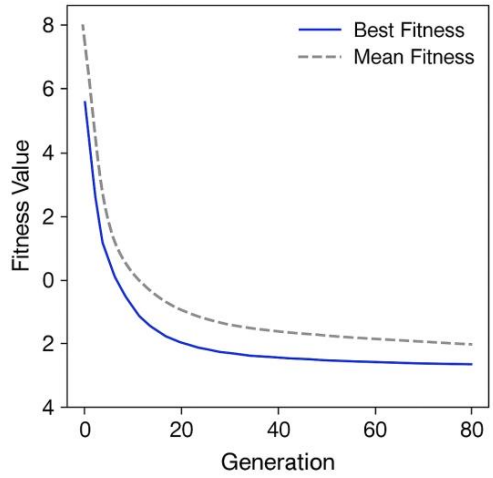

Fig. 15. Convergence curve of the GA, showing the evolution of the best fitness value over successive generations.

results demonstrate that the proposed state-feedback stabilizer maintains superior damping characteristics, reducing rotor-speed and rotor-angle oscillations by approximately 40–60% compared with the base case and achieving faster voltage recovery at the PCC.

Figs. 11 and 12 depict the rotor angle deviation ($\Delta\delta$) responses under 10% and 20% mechanical input perturbations, respectively. In the absence of the stabilizer, the rotor angle exhibits sustained oscillations with a large amplitude, indicating poor synchronizing torque and weak electromechanical coupling between the generator and inverter subsystems.

By applying the proposed state-feedback controller, both the amplitude and duration of the angle oscillations are significantly reduced. The proposed control law effectively injects a supplementary damping torque that enhances the synchronizing power coefficient, thereby improving angular stability. As a result, the rotor angle deviation settles rapidly with negligible residual oscillations, preventing phase divergence and maintaining synchronism among the microgrid units.

To provide a more quantitative comparison of the dynamic responses shown in Figs. 9–11, several standard time-domain evaluation indices were computed, including the Integral of Absolute Error (IAE), the Integral of Squared Error (ISE), and the Integral of Time-weighted Absolute Error (ITAE). Table 8 summarizes these indices for the rotor-speed and rotor-angle deviations under a 10% step disturbance. The results show that the proposed GA-optimized state-feedback controller significantly reduces all performance metrics, indicating faster convergence, reduced oscillation energy, and improved transient quality.

The excitation voltage responses (ΔE_{fd}), presented in Figs. 12 and 13, reveal the dynamic behavior of the diesel generator's excitation system under the same disturbance conditions. Without the proposed stabilizer, the field voltage experiences large and sustained oscillations, causing voltage fluctuations at the point of common coupling. The addition of the optimized state-feedback controller introduces an adaptive corrective signal through the Automatic Voltage Regulator (AVR) loop, resulting in a smoother excitation voltage trajectory and faster convergence to the steady-state value. For both the 10% and 20% disturbances, the proposed controller reduces the maximum deviation of E_{fd} by approximately 45–55% and eliminates residual oscillations within 1 second after the disturbance. This demonstrates that the feedback mechanism not only stabilizes the rotor dynamics but also enhances voltage regulation and excitation system damping.

As shown in Fig. 15, the best fitness value rapidly decreases during the first 20–25 generations, followed by a gradual refinement stage, converging to a stable minimum after approximately 60–70 generations. This behavior confirms the efficiency of the GA in exploring the search space and achieving robust optimization for the proposed control framework.

The comparative results across all six figures indicate that the proposed GA-optimized state-feedback controller significantly enhances both transient and small-signal stability of the islanded microgrid. The controller successfully mitigates electromechanical oscillations, reduces overshoot, and improves both speed and voltage recovery following step changes in mechanical input. These findings confirm that the coordinated tuning of the inverter control loops and the diesel generator's stabilizer yields superior damping performance, ensures robustness to load variations, and improves overall dynamic stiffness of the system. In summary, the time-domain results fully corroborate the eigenvalue analysis presented in this section, verifying that the proposed control approach provides an effective and reliable stabilization mechanism for islanded microgrids. The quantitative results in Table 9 clearly show that the proposed state-feedback stabilizer significantly reduces peak deviations and overshoot while accelerating settling time for both disturbance levels. For example, in the 10% disturbance case, the settling time is reduced by approximately 68%, and the overshoot decreases by about 60%. Similar improvements are observed for the 20% disturbance, confirming consistent damping enhancement across different operating conditions.

Overall, the controller exhibited consistent performance across mechanical disturbances and load variations, indicating robustness to different operating conditions. Additional inverter-level disturbances (e.g., voltage-reference perturbations) are

Table 9. Quantitative performance comparison for 10% and 20% disturbances.

Disturbance	Case	Peak deviation ($\Delta\omega_{\max}$)	Overshoot (%)	Settling time (s)	Improvement vs baseline
10% Step	Without SFC	0.047 pu	100	3.8	—
10% Step	With SFC	0.019 pu	59	1.2	Settling time ↓ 68%
20% Step	Without SFC	0.091 pu	100	4.6	—
20% Step	With SFC	0.038 pu	58	1.4	Settling time ↓ 70%

Table 10. Frequency-domain stability indicators of the diesel generator–AVR loop.

Case	Gain margin, GM (dB)	Phase margin, PM (deg)	Gain crossover Freq. (rad/s)	Phase crossover Freq. (rad/s)
Without SFC	4.1	17	12.5	7.8
With GA-optimized SFC	10.6	42	18.3	11.2

identified as a direction for future work, although the new load-variation test already validates the controller's effectiveness under a broader range of system conditions. As shown in Table 10, the proposed state-feedback controller more than doubles both gain and phase margins, indicating a substantially more robust closed-loop behavior in the frequency domain.

6. CONCLUSION

The results obtained from the eigenvalue analysis and time-domain simulations validate the effectiveness of the GA-optimized state-feedback controller in improving the stability and dynamic performance of the islanded microgrid. The eigenvalue analysis demonstrated a significant shift of the system's eigenvalues toward the left half of the complex plane, indicating improved damping and reduced low-frequency oscillations, which enhances the small-signal stability of the system. In the time-domain simulations, the system's response to step changes in mechanical power showed a marked improvement in terms of damping, settling time, and voltage regulation when the state-feedback controller was applied. The rotor speed, rotor angle, and field voltage deviations were significantly reduced, with faster decay rates and lower overshoot observed compared to the base case without the feedback controller. This indicates that the proposed controller not only enhances dynamic performance but also improves robustness under varying operating conditions, ensuring stable operation of the diesel generator and inverter subsystems. Overall, the coordinated tuning of the inverter-based DG controllers and the state-feedback power system stabilizer offers a reliable and effective solution to mitigate oscillatory behavior, improve damping, and ensure robustness in islanded microgrids, making it a viable control strategy for modern power systems with distributed generation. Quantitatively, the proposed GA-optimized state-feedback stabilizer increases the damping ratio of the dominant electromechanical mode from approximately 0.03 to 0.18, corresponding to a sixfold improvement. The peak rotor-speed deviation under a 10% mechanical disturbance decreases by nearly 60%, and the settling time is reduced by about 70%. Similar improvements are observed for the 20% disturbance and for the load-variation scenario, confirming consistent enhancement across multiple operating conditions. While the proposed stabilizer demonstrates strong performance, several limitations remain. The controller relies on accurate linearization around a nominal operating point, and its performance may vary under large disturbances or nonlinear saturation effects. Communication delays, measurement noise, and practical constraints in estimating internal generator states were not explicitly modeled. Future work may extend the controller to nonlinear or adaptive frameworks, incorporate inverter-side disturbances, and validate the approach experimentally on hardware-in-the-loop or microgrid testbeds.

ACKNOWLEDGEMENT

The authors acknowledge the use of artificial intelligence tools (e.g., ChatGPT by OpenAI) for language editing and clarity improvement during the preparation of this manuscript. The authors are fully responsible for the scientific content, analysis, and conclusions.

REFERENCES

[1] M. Rezaee, R. Fathi, and V. A. Maleki, "Dynamic analysis and uncertainty modeling of viscoelastic beam response to fluid stimulation: Insights into nonlinear effects and velocity uncertainties," *Appl. Ocean Res.*, vol. 157, p. 104487, 2025.

[2] E. Uchkun, M. Axmedovich, K. Boburmirzo, L. Tadjibaeva, S. Nasirova, D. Djonikulovna, and A. Azamat, "The impact of clean fuel technology in the transportation system to reduce pollution," *Procedia Environ. Sci. Eng. Manag.*, vol. 12, no. 1, pp. 81–88, 2025.

[3] M. Nasrabadi, A. V. Sevbitov, V. A. Maleki, N. Akbar, and I. Javanshir, "Passive fluid-induced vibration control of viscoelastic cylinder using nonlinear energy sink," *Mar. Struct.*, vol. 81, p. 103116, 2024.

[4] A. Nazori, G. Triyono, G. Brotosaputro, D. Mahdiana, and S. Solichin, "The use of artificial intelligence in the development of clean energy for the transportation industry," *Procedia Environ. Sci. Eng. Manag.*, vol. 11, pp. 27–36, 2024.

[5] N. Rehman, M. Mufti, and N. Gupta, "Power flow analysis in a distribution system penetrated with renewable energy sources: A review," *Int. J. Ambient Energy*, vol. 45, no. 1, p. 2305701, 2024.

[6] L. Strezoski, "Advances in power and energy management for distribution systems with high penetration of distributed energy resources," *Energies*, vol. 18, no. 3, pp. 723–732, 2025.

[7] P. Wang, H. Zhao, J. Luo, and V. Terzija, "Low-frequency impedance modeling of wind energy conversion system considering mechanical dynamics and operating regions," *J. Mod. Power Syst. Clean Energy*, vol. 8, pp. 67–76, 2024.

[8] A. Nazori, G. Brotosaputro, S. Solichin, U. Budiyanto, and D. Mahdiana, "Design and implementation of fuzzy intelligent controller to manage energy resources in a greenhouse system," *Procedia Environ. Sci. Eng. Manag.*, vol. 11, no. 1, pp. 19–25, 2024.

[9] F. Al Sharari, O. Yemelyanov, Y. Dziurakh, O. Sokil, and O. Danylovych, "The energy-saving projects' impact on the level of an enterprise's financial stability," *Econ. Ann.-XXI*, vol. 195, no. 1–2, pp. 36–49, 2022.

[10] M. Yadipour, F. Hashemzadeh, and M. Baradarannia, "A novel strategy to enlarge the domain of attraction of affine nonlinear systems," *Itogi Nauki Tekh. Sovrem. Mat. Prilozh. Temat. Obz.*, vol. 178, pp. 91–101, 2020.

[11] M. Yadipour, F. Hashemzadeh, and M. Baradarannia, "A novel strategy of extending the domain of attraction of affine nonlinear systems," *J. Math. Sci.*, vol. 276, no. 2, pp. 289–299, 2022.

[12] S. Nandanoori, S. Kundu, W. Du, F. K. Tuffner, and K. P. Schneider, "Distributed small-signal stability conditions for inverter-based unbalanced microgrids," *IEEE Trans. Power Syst.*, vol. 35, no. 5, pp. 3981–3990, 2020.

[13] H. Hosseinpour, M. MansourLakouraj, M. Benidris, and H. Livani, "Large-signal stability analysis of inverter-based AC microgrids: A critical and analytical review," *IEEE Access*, vol. 11, pp. 111466–111491, 2023.

[14] I. Davoudkhani, P. Zare, A. Y. Abdelaziz, M. Bajaj, and M. B. Tuka, "Robust load-frequency control of islanded urban microgrid using 1pd-3dof-pid controller including mobile ev energy storage," *Sci. Rep.*, vol. 14, no. 1, p. 13962, 2024.

[15] A. Oshnoei, M. A. Azzouz, A. S. Awad, F. Blaabjerg, and A. Anvari-Moghaddam, "Adaptive damping control to enhance small-signal stability of DC microgrids," *IEEE J. Emerg. Sel. Top. Power Electron.*, vol. 11, no. 3, pp. 2963–2978, 2024.

[16] A. Krismanto, N. Mithulananthan, R. Shah, H. Setiadi, and M. R. Islam, "Small-signal stability and resonance perspectives in microgrid: A review," *Energies*, vol. 16, no. 3, pp. 1017–1022, 2023.

[17] R. Sebastián, "Review on dynamic simulation of wind diesel isolated microgrids," *Energies*, vol. 14, no. 7, pp. 1812–1823, 2023.

[18] A. Tang, X. Wu, T. Xu, Y. Hu, S. Long, and Q. Yu, "State of health estimation based on inconsistent evolution for lithium-ion battery module," *Energy*, vol. 286, p. 129575, 2024.

[19] T. Kerdphol, F. S. Rahman, M. Watanabe, Y. Mitani, D. Turschner, and H.-P. Beck, "Enhanced virtual inertia control based on derivative technique to emulate simultaneous inertia and damping properties for microgrid frequency regulation," *IEEE Access*, vol. 7, pp. 14422–14433, 2019.

[20] H. Ranjbar, M. Kazemi, N. Amjady, H. Zareipour, and S. H. Hosseini, "Maximizing the utilization of existing grids for renewable energy integration," *Renew. Energy*, vol. 189, pp. 618–629, 2022.

[21] B. Khokhar, K. S. Parmar, T. Thakur, and D. P. Kothari, *Load Frequency Control of Microgrids*. CRC Press, 2024.

[22] A. Daraz, "Optimized cascaded controller for frequency stabilization of marine microgrid system," *Appl. Energy*, vol. 350, p. 121774, 2023.

[23] T. H. Meles and L. Ryan, "Adoption of renewable home heating systems: An agent-based model of heat pumps in ireland," *Renew. Sustain. Energy Rev.*, vol. 169, p. 112853, 2024.

[24] H. Shayeghi, A. Rahnama, and H. Mojarad, "Designing a multi-objective optimized parallel process controller for frequency stabilization in an islanded microgrid," *J. Oper. Autom. Power Eng.*, vol. 5, pp. 89–94, 2025.

[25] H. Shayeghi, A. Rahnama, N. Bizon, and A. Szumny, "Interconnected microgrids load-frequency control using stage-by-stage optimized TIDA+1 error signal regulator," *Eng. Rep.*, vol. 7, no. 1, p. e13095, 2025.

[26] G. Liu, W. Ma, and Y. Zhang, "An anti-windup and backlash compensation-based finite-time control method for performance enhancement of a class of nonlinear systems," *Asian J. Control*, vol. 26, no. 4, pp. 1864–1880, 2024.

[27] A. Pourasghar, E. Mehdizadeh, T. C. Wong, A. K. Hoskoppal, and J. C. Brigham, "A computationally efficient approach for estimation of tissue material parameters from clinical imaging data using a level set method," *J. Eng. Mech.*, vol. 150, no. 10, p. 04024075, 2024.

[28] K. Bingham, S. Sourani Yancheshmeh, G. Vaidya, A. Ebrahimpour, and T. Deemyad, "Advanced material selection and design strategies for optimized robotic systems," in *Proc. ASME Int. Mech. Eng. Congr. Expo. (IMECE)*, American Society of Mechanical Engineers, 2024.

[29] S. Sourani Yancheshmeh, A. Ebrahimpour, and T. Deemyad, "Optimizing chassis design for autonomous vehicles in challenging environments based on finite element analysis and genetic algorithm," in *Proc. ASME Int. Mech. Eng. Congr. Expo. (IMECE)*, American Society of Mechanical Engineers, 2024.

[30] J. Tao, L. Meng, J. Han, Q. Yang, W. Li, and Y. Guo, "Dynamic modeling and electromechanical coupling characteristics analysis in diesel generator set," *J. Vib. Eng. Technol.*, vol. 13, no. 8, p. 612, 2025.

[31] Q. Liu, P. Chen, S. Liu, C. Wang, and J. Liu, "A topology and control method for operational testing of $\pm$800 kv/8 GW flexible DC transmission modular multilevel converter valve," *IEEE Access*, vol. 12, pp. 55669–55681, 2024.

[32] A. Pilloni, A. Pisano, and E. Usai, "Robust finite-time frequency and voltage restoration of inverter-based microgrids via sliding-mode cooperative control," *IEEE Trans. Ind. Electron.*, vol. 65, no. 1, pp. 907–917, 2018.